UNITED NATIONS EDUCATIONAL, SCIENTIFIC AND CULTURAL ORGANIZATION
INTERNATIONAL ATOMIC ENERGY AGENCY
INTERNATIONAL CENTRE FOR THEORETICAL PHYSICS

SMR/917 - 3

SECOND WORKSHOP ON SCIENCE AND TECHNOLOGY OF THIN FILMS

(11 - 29 March 1996)

Reading material about:
" Nanoelectronic properties of thin films "

presented by:

R. WIESENDANGER
Universität Hamburg
Institut für Angewandte Physik
Jungiusstrasse 11
D-20355 Hamburg
Germany

To appear in:
Handbook of Microscopy
VCH Weinheim 1996

General Introduction

Scanning near-field probe microscopy (SNPM) has developed from scanning tunneling microscopy (STM), which was invented in 1981 by G. Binnig, H. Rohrer, Ch. Gerber, and E. Weibel at the IBM Zürich Research Laboratory [1–3]. SNPM combines three important concepts: scanning, point probing, and near-field operation [4]. Scanning is achieved by means of piezoelectric drives which allow the positioning and raster scanning of a point probe relative to a sample surface to be investigated with subatomic accuracy. Nonlinearities due to piezoelectric hysteresis and creep usually have to be corrected electronically or by software to prevent image distortions. Point probing allows local information to be obtained about the physical and chemical properties of a sample surface, which facilitates the investigation of site-specific sample properties. The point probe is brought in close proximity to the sample at a distance s which is smaller than some characteristic wavelength λ of a particular type of interaction between the probe tip and the sample. [In the case of STM, λ would be the electron wavelength whereas for scanning near-field optical microscopy (SNOM), λ would be the optical wavelength.] In this so-called near-field regime (where $s \leqslant \lambda$), the spatial resolution that can be achieved is no longer limited by diffraction, but rather by geometrical parameters: the distance s between the point probe and the sample surface, and the effective radius of curvature R of the point probe. SNPM is therefore an exceptional type of microscopy because it works without lenses (in contrast to optical and electron microscopy), and achieves 'super resolution' beyond the Abbé limit. Another important feature of SNPM is that it can be operated in air and in liquids as well as in vacuum, which offers novel opportunities for high-resolution studies of the structure and processes at solid/fluid interfaces. In particular, in situ electrochemical studies and in vivo investigations of biological specimens at unprecedented real-space resolutions have become some of the more recent intense fields of application, besides surface science studies under ultra-high-vacuum conditions.

1 Scanning Tunneling Microscopy

1.1 Introduction

Scanning tunneling microscopy (STM) was the first near-field microscopy technique to be developed. It is based on vacuum tunneling of electrons between an electrically conducting point probe and an electrically conducting sample (metal or doped semiconductor). The schematic set-up for an STM experiment is shown in Fig. 1. An atomically sharp probe tip is brought within a distance of only a few angstroms ($1\,\text{Å} = 0.1\,\text{nm} = 10^{-10}\,\text{m}$) from a sample surface by means of a piezoelectric drive in the z-direction (normal to the sample surface). If a bias voltage U has been applied between the tip and sample, a tunneling current I will flow due to the quantum mechanical tunneling effect even before mechanical point contact is reached. Since the tunneling current

Further reading: see reference [4].

is strongly (exponentially) dependent on the tip–surface separation, it can be used very efficiently for distance control. By scanning the tip over the sample surface while keeping the tunneling current constant by means of an electronic feedback circuit, the surface contours can be traced by the tip. A quasi-three-dimensional 'topographic' image $z(x,y)$ of the sample surface is gained by monitoring the vertical position z of the tip as a function of the lateral position (x,y), which is controlled by piezoelectric drives in the x- and y-directions. The position (x,y,z) of the tip can be calculated based on the known sensitivities of the piezoelectric drives in the x-, y-, and z-directions and the corresponding driving voltages U_x, U_y, and U_z.

In addition to its use to control the tip–surface separation, the tunneling current contains valuable information about the local electronic properties of the sample surface and—to some extent—of the tip as well, which is unwanted in most cases. In the following, constant-current topographs and the various dependencies on experimental and sample-specific parameters will systematically be discussed. This will allow classification of the information which can be extracted from STM experiments.

1.2 'Topographic Imaging' in the Constant-Current Mode

Within Bardeen's transfer Hamiltonian formalism [5], the tunneling current I can be evaluated from the first-order time-dependent perturbation theory according to

$$I = \frac{2\pi e}{\hbar}\sum_{\mu,\nu}[f(E_\mu)(1-f(E_\nu+eU)) - f(E_\nu+eU)(1-f(E_\mu))] \times |M_{\mu,\nu}|^2\delta(E_\nu - E_\mu) \quad (1)$$

where $f(E)$ is the Fermi function, U is the applied sample bias voltage, $M_{\mu,\nu}$ is the tunneling matrix element between the unperturbed electronic states ψ_μ of the tip and ψ_ν of the sample surface, and $E_\mu(E_\nu)$ is the energy of the state $\psi_\mu(\psi_\nu)$ in the absence of tunneling. The delta function describes the conservation of energy for the case of elastic tunneling. (Inelastic tunneling will be considered later; see Sec. 1.6.) The essential problem is the calculation of the tunneling matrix element which, according to Bardeen [5], is given by

$$M_{\mu,\nu} = \frac{\hbar^2}{2m}\int \mathrm{d}S\,(\psi_\mu^*\nabla\psi_\nu - \psi_\nu\nabla\psi_\mu^*) \quad (2)$$

where the integral has to be evaluated over any surface lying entirely within the vacuum barrier region separating the two electrodes. The quantity in parentheses can be identified as a current density $j_{\mu,\nu}$. To derive the matrix element $M_{\mu,\nu}$ from Eq. (2), explicit expressions for the wave functions ψ_μ and ψ_ν of the tip and sample surface are required. Unfortunately, the atomic structure of the tip is generally not known. Therefore, a model tip wave function has to be assumed for calculation of the tunneling current.

Tersoff and Hamann [6, 7], who first applied the transfer Hamiltonian approach to STM, used the simplest possible model for the tip with a local spherical symmetry. In this model, the tunneling matrix element is evaluated for a s-type tip wave function, whereas con-

tributions from tip wave functions with angular dependence (orbital quantum number $l \neq 0$) have been neglected. Tersoff and Hamann considered the limits of low temperature and small applied bias voltage, for which the tunneling current becomes

$$I = \frac{2\pi e}{\hbar} U \sum_{\mu,\nu} |M_{\mu,\nu}|^2 \times \delta(E_\nu - E_F)\delta(E_\mu - E_F) \quad (3)$$

where E_F is the Fermi energy. Within the s-wave approximation for the tip, the following expression for the tunneling current is finally obtained

$$I \propto U n_t(E_F) \exp(2\kappa R) \times \sum_\nu |\psi_\nu(\bar{r}_0)|^2 \delta(E_\nu - E_F) \quad (4)$$

with the decay rate $\kappa = (2m\phi)^{1/2}/\hbar$, where ϕ is the density of states at the Fermi level for the tip, R is the effective tip radius, and $\bar{r}_0$ is the center of curvature of the tip. The quantity

$$n_s(E_F, \bar{r}_0) = \sum_\nu |\psi_\nu(\bar{r}_0)|^2 \delta(E_\nu - E_F) \quad (5)$$

can be identified with the surface local density of states (LDOS) at the Fermi level E_F, that is, the charge density from electronic states at E_F, evaluated at the center of curvature r of the effective tip. The STM images obtained at low bias in the constant-current mode therefore represent contour maps of constant surface LDOS at E_F evaluated at the center of curvature of the effective tip, provided that the s-wave approximation for the tip can be justified. Since the wave functions decay exponentially in the z-direction normal to the surface toward the vacuum region,

$$\psi_\nu(\bar{r}) \propto \exp(-\kappa z) \quad (6)$$

it follows that

$$|\psi_\nu(\bar{r}_0)|^2 \propto \exp[-2\kappa(s + R)] \quad (7)$$

where s denotes the distance between the sample surface and the front end of the tip. Therefore, the tunneling current, given by Eq. (4), becomes exponentially dependent on the distance s, as mentioned in the introduction:

$$I \propto \exp(-2\kappa s) \quad (8)$$

The strong exponential distance dependence typically leads to an order-of-magnitude increase in the tunneling current for each angstrom decrease in the tip–surface separation.

Unfortunately, the simple interpretation of constant current STM images as given by Tersoff and Hamann is not valid for high bias or for tip wave functions with angular dependence.

1.2.1 Effects of Finite Bias

The applied bias voltage enters through the summation of states which can contribute to the tunneling current. Additionally, a finite bias can lead to a distortion of the tip and sample surface wave functions ψ_μ and ψ_ν as well as to a modification of the energy eigenvalues E_μ and E_ν [8]. The derivation of these distorted tip and sample surface wave functions and energy eigenvalues under the presence of an applied bias is, however, a difficult problem. Therefore, as a first approximation, the undistorted zero-voltage wave functions and energy eigenvalues are usually taken. Consequently, the effect of a finite bias U only enters through a shift in energy of the undistorted surface wave functions

or density of states relative to the tip by an amount eU. Under this approximation, the following expression for the tunneling current as a generalization of the result of Tersoff and Hamann may be used:

$$I \propto \int_0^{eU} n_t(\pm eU \pm \mathscr{E}) n_s(\mathscr{E}, \bar{r}_0)\, d\mathscr{E} \qquad (9)$$

where $n_t(\mathscr{E})$ is the density of states for the tip and $n_s(\mathscr{E}, \bar{r}_0)$ is the density of states for the sample surface evaluated at the center of curvature $\bar{r}_0$ of the effective tip. All energies $\mathscr{E}$ are measured with respect to the Fermi level. One can now make the following approximation motivated by a generalization of Eq. (5) together with Eq. (7):

$$n_s(\mathscr{E}, \bar{r}_0) \propto n_s(\mathscr{E}) \exp\left\{-2(s+R) \times \left[\frac{2m}{\hbar^2}\left(\frac{\phi_t + \phi_s}{2} + \frac{eU}{2} - \mathscr{E}\right)\right]^{1/2}\right\} \qquad (10)$$

where a WKB-type expression for the decay rate κ in the exponential term has been used. $\phi_t(\phi_s)$ denotes the tip (sample surface) work function. Finally, one obtains

$$I \propto \int_0^{eU} n_t(\pm eU \pm \mathscr{E}) n_s(\mathscr{E}) T(\mathscr{E}, eU)\, d\mathscr{E} \qquad (11)$$

with an energy- and bias-dependent transmission coefficient $T(\mathscr{E}, eU)$ given by

$$T(\mathscr{E}, eU) = \exp\left\{-2(s+R) \times \left[\frac{2m}{\hbar^2}\left(\frac{\phi_t + \phi_s}{2} + \frac{eU}{2} + \mathscr{E}\right)\right]^{1/2}\right\} \qquad (12)$$

In Eqs. (11) and (12), matrix element effects in tunneling are expressed in terms of a modified decay rate κ including a dependence on energy E and applied bias voltage U. The expression (12) for the transmission coefficient neglects image potential effects as well as the dependence of the transmission probability on parallel momentum. This can be included by an increasingly more accurate approximation for the decay rate κ.

1.2.2 Effects of Tip Wave Functions with Angular Dependence

STM tips are usually made from tungsten or platinum–iridium alloy wire. For these materials, the density of states at the Fermi level is dominated by d-states rather than by s-states. Indeed, first-principle calculations of the electronic states of several types of tungsten clusters used to model the STM tip revealed the existence of dangling-bond states near the Fermi level at the apex atom which can be ascribed to d_{z^2} states [9]. Evaluation of the tunneling current according to Eqs. (1) and (2) now requires calculation of the tunneling matrix element for tip wave functions with angular dependence ($l \neq 0$). Chen [10] has shown that generally the tunneling matrix element can simply be obtained from a 'derivative rule'. The angle dependence of the tip wave function in terms of x, y, and z has to be replaced according to

$$x \rightarrow \frac{\partial}{\partial x}, \quad y \rightarrow \frac{\partial}{\partial y}, \quad z \rightarrow \frac{\partial}{\partial z} \qquad (13)$$

where the derivatives have to act on the sample surface wave function at the center of the apex atom. For instance, the tunnel-

ing matrix element for a p_z tip state is proportional to the z-derivative of the sample surface wave function at the center of the apex atom at r_0.

In terms of a microscopic view of the STM imaging mechanism [11] illustrated in Fig. 2, a dangling-bond state at the tip apex atom is scanned over a two-dimensional array of atomic-like states at the sample surface. Overlap of the tip state with the atomic-like states on the sample surface generates a tunneling conductance which depends on the relative position of the tip state and the sample state. The atomic corrugation Δz depends on the spatial distribution as well as on the type of tip and sample surface states. Generally, for non-s-wave tip states, the tip apex atom follows a contour, determined by the derivatives of the sample surface wave functions, which exhibit much stronger atomic corrugation than the contour of constant surface LDOS at E_F.

1.2.3 Imaging of Adsorbates

The transfer Hamiltonian approach as used by Tersoff and Hamann has further limitations. First, it is a perturbative treatment of tunneling, being appropriate only for weakly overlapping electronic states of the two electrodes. Secondly, this approach suffers from the fact that assumptions for the tip and sample surface wave functions have to be made in order to derive the tunneling current.

As an alternative, Lang [12, 13] has calculated the tunneling current between two planar metal electrodes with adsorbed atoms where the wave functions for the electrodes have been obtained self-consistently within density functional theory. In Fig. 3a the calculated current density distribution from a single sodium atom adsorbed at its equilibrium distance on one of the two metal electrodes is shown. The plot illustrates how spatially localized the tunneling current is. By scanning one adsorbed atom (taken as the tip) past another adsorbed atom (taken as the sample), the vertical tip displacement versus the lateral position can be evaluated under the constant-current condition [13]. In Fig. 3b, constant-current scans at low bias of a sodium tip atom past three different sample adatoms (sodium, sulfur, and helium) are shown. Most striking is the negative tip displacement for adsorbed helium. The closed valence shell of helium is very much lower in energy with respect to the Fermi level, and its only effect is to polarize metal states away from E_F, thereby producing a decrease in the Fermi level state density. This results in a reduced tunneling current flow, that is, a negative tip displacement in a constant-current scan. This example illustrates nicely that 'bumps' or 'holes' in 'topographic' STM images may not correspond to the presence or absence of surface atoms, respectively—sometimes even the reverse is true.

1.2.4 Spatial Resolution in Constant-Current Topographs

According to Tersoff and Hamann [7], an STM corrugation amplitude, or corrugation in brief, Δ, may be defined by

$$\Delta := z_+ - z_- \tag{14}$$

where z_+ and z_- denote the extremal

values of the z-displacement of the tip in a constant-current scan. This corrugation Δ decreases exponentially with distance z from the surface,

$$\Delta \propto \exp(-\gamma z) \tag{15}$$

where the decay rate γ is very sensitive to the surface lattice constant because it depends quadratically on the corresponding Fourier component G in the expansion of the surface charge density,

$$\gamma \propto \tfrac{1}{4}\kappa^{-1}G^2 \tag{16}$$

with $\kappa^2 = 2m\phi/\hbar^2$. Consequently, only the lowest non-zero Fourier component determines the corrugation at sufficiently large distances. Tersoff and Hamann [6, 7] argued that suppression of higher Fourier components in their expression for the tunneling current between a spherical tip of radius R and a sample surface at a distance s from the front end of the tip is equivalent to a spatial resolution determined by

$$\left(\frac{R+s}{\kappa}\right)^{1/2} \tag{17}$$

According to this expression, the lateral resolution in STM is determined by the geometrical parameters R and s, rather than by the wavelength of the tunneling electrons. This is characteristic for near-field microscopes which are operated at distances between the probe tip and the sample surface that are small compared with the wavelength, as mentioned in the introduction. For STM, typical tip–surface separations are 3–10 Å, whereas the wavelength of tunneling electrons typically varies in the range 12–120 Å for an applied bias voltage of 0.01–1 V.

The expression, Eq. (17), for the lateral resolution in constant-current STM images implies that high spatial resolution is obtained with a small radius of curvature of the effective tip and at a small tip–surface separation, that is, at low tunneling gap resistance. Both dependencies have been verified experimentally. The dependence of the measured corrugation on the radius of curvature of the effective tip was studied by combined STM–FIM (field ion microscopy) experiments [15] where the obtained STM results could be correlated directly with the size of the effective tip as revealed by FIM (Fig. 4). As a direct consequence, measured absolute values for the corrugation Δ are meaningless if the microscopic structure of the tip is not known.

The dependence of the measured corrugation on the tip–surface separation has experimentally been studied by systematic variation of the tunneling gap resistance [16, 17]. In particular, the suppression of higher Fourier components in the expansion of the surface charge density with increasing tip–surface separation, as theoretically predicted by Tersoff and Hamann [6, 7], has experimentally been verified [17]. Figure 5 shows the influence of the chosen tip–surface separation on the spatial resolution achieved on a W(110)/C-(15 × 3) reconstructed surface. It is immediately apparent that the STM results can critically depend on the tip–surface separation, that is, on the tunneling gap resistance, particularly for surface structures with complex unit cell structure.

For close-packed metal surfaces, such as Au(111) [18] or Al(111) [16], atomic resolution could not be explained within the spherical tip model employed by Tersoff and Hamann. Baratoff [19] early on pointed out that the spatial resolution might be considerably improved compared

with expression (17) if tunneling occurs via localized surface states or dangling bonds. Later, Chen [11, 20] systematically investigated the influence of different tip orbitals on the spatial resolution within a microscopic view of STM. The calculated enhancement of the tunneling matrix element by tip states with $l \neq 0$ was shown to lead to increased sensitivity to atomic-sized features with large wavevectors. For instance, a p_z tip state acts as a quadratic high-pass filter, whereas a d_{z^2} tip state acts as a ~~quadratic~~ quartic high-pass filter. Consequently, the resolution of STM can be considerably higher than predicted within the s-wave tip model. The spontaneous switching of the resolution often observed in or between atomic-resolution STM images can be explained by the fact that a very subtle change of the tip involving a change of the effective orbital can induce a tremendous difference in STM resolution. In conclusion, it is the orbital at the front end of the tip which mainly determines the spatial resolution in STM. A p_z orbital typical for elemental semiconductors or a d_{z^2} orbital from d-band metals are most favorable. Therefore, 'tip-sharpening procedures' have to aim at bringing such favorable orbitals to the front of the tip [11].

1.3 Local Tunneling Barrier Height

According to Eq. (8), the tunneling current I was found to depend exponentially on the tip–surface separation s:

$$I \propto \exp(-2\kappa s)$$

with a decay rate κ given by

$$\kappa = \frac{(2m\phi)^{1/2}}{\hbar}$$

where ϕ is an effective local potential barrier height. So far, ϕ was assumed to be laterally uniform. In reality, ϕ exhibits spatial variations which can yield additional information about the sample surface under investigation.

Motivated by Eq. (8), an apparent local barrier height is usually defined by

$$\phi_A = \frac{\hbar^2}{8m}\left(\frac{d \ln I}{ds}\right)^2 \tag{18}$$

For large tip–surface separations outside the effective range of image forces, it is clear that ϕ has to approach the surface local work function ϕ_s, which is defined as the work needed to remove an electron from the Fermi level of the solid to a position somewhat outside of the surface where image force effects can be neglected. However, for small tip–surface separations (5–10 Å), image potential effects certainly have to be considered. By assuming a model potential [21]

$$\phi(d) = \phi_0 - \frac{\alpha}{d} \tag{19}$$

where ϕ_0 is the average work function of the sample surface and the probe tip $[\phi_0 = (\phi_s + \phi_t)/2]$, and d is the distance between the two image planes $(d \approx s - 1.5\,\text{Å})$, the distance dependence of the tunneling current can be calculated:

$$\frac{d \ln I}{ds} = -\frac{2(2m)^{1/2}}{\hbar} \times \phi_0^{1/2}\left[1 + \frac{\alpha^2}{8\phi_0^2 d^2} + \mathcal{O}\left(\frac{1}{d^3}\right)\right] \tag{20}$$

As can be seen from Eq. (20), the first-order term in $1/d$, although present in the

potential $\phi(d)$, cancels exactly in the expression for $\mathrm{d}\ln I/\mathrm{d}s$. The second-order term in $1/d$ usually contributes only a few percent of the zero-order term and can therefore be neglected to a first approximation. As a consequence, one finds

$$\frac{\mathrm{d}\ln I}{\mathrm{d}s} \approx \text{const.} \tag{21}$$

and

$$\phi_A \approx \phi_0 = \text{const.}$$

This means that the presence of the image potential does not show up in the distance dependence of the tunneling current although the absolute values of the current are drastically affected by the presence of the image potential. The distance independence of the apparent barrier height deduced from the $\ln I$–s relation (Fig. 6) has been verified experimentally as well as by more detailed theoretical analysis [22].

1.3.1 Local Tunneling Barrier Height Measurements at Fixed Surface Locations

According to Eq. (18), the apparent barrier height ϕ_A can be determined locally by measuring the slope of $\ln I$–s characteristics at a fixed sample bias voltage U and at a fixed sample surface location. To demonstrate vacuum tunneling it is necessary to obtain reasonably high values for ϕ_A of several electronvolts in addition to verifying the exponential dependence of the current on the tip–surface separation.

Alternatively, the apparent barrier height can be deduced from the slope of local $\ln U$–s characteristics in a low applied bias voltage range and at a fixed tunneling current. In the low-bias regime, the tunnel junction exhibits Ohmic behavior, as found earlier (4):

$$I \propto U \exp(-2\kappa s) \tag{22}$$

Therefore, one obtains

$$\phi_A = \frac{\hbar^2}{8m}\left(\frac{\mathrm{d}\ln U}{\mathrm{d}s}\right)^2 \tag{23}$$

at constant current.

1.3.2 Spatially Resolved Local Tunneling Barrier Height Measurements

The experimental determination of the spatially resolved local tunneling barrier height $\phi_A(x, y)$ can be performed by modulating the tip–surface separation s by Δs while scanning at a constant average current I, with a modulation frequency ν_0 higher than the cut-off frequency of the feedback loop [23]. The modulation of $\ln I$ at ν_0 can be measured by a lock-in amplifier simultaneously with the corresponding constant-current topograph, and directly yields a signal proportional to the square root of the apparent barrier height via the relation

$$\frac{\Delta \ln I}{\Delta s} = -\frac{2\sqrt{2m}}{\hbar}\sqrt{\phi_A} \tag{24}$$

The apparent barrier height obtained in this way is not measured at a constant tip–surface separation s. Scanning at a constant average current (and at a constant applied bias voltage) implies that the product $\sqrt{\phi_A}s$ is kept constant, rather than s. However, since the spatial variation of ϕ_A is usually small (about 10% or less of the absolute value of ϕ_A), and ϕ_A enters only

under the square root, the spatial variation of $\phi_A(x, y)$ is usually measured almost at a constant tip–surface separation s.

Spatially resolved measurements of the apparent potential barrier height can yield information about spatial inhomogeneities of the local sample work function ϕ_s, which can be split into two contributions. The chemical component of ϕ_s is determined by the chemical nature and structure of the solid only, whereas the electrical component of ϕ_s depends on the chemical nature of the solid as well as on the surface crystallographic orientation. Therefore, spatially resolved measurements of ϕ_A can be used, for instance, to map chemical inhomogeneities at surfaces as well as different crystallographic facets of small crystallites.

On the atomic scale, it is more appropriate to relate the measured apparent barrier height with the decay rates of the wave functions describing the sample surface and the tip. Lateral variations of $\phi_A(x, y)$ then have to be interpreted as lateral variations in the decay rate of the surface wave function. As we know from Eq. (15), the measured surface atomic corrugation Δ in constant-current STM images is smoothed out exponentially with an increasing tip–surface separation s. This can only occur if the decay rate κ_p above a local protrusion in the topography is larger than the decay rate κ_d above a local depression. Consequently, the apparent barrier height above a local topographic protrusion has to be larger than the barrier height above a local depression. Therefore, atomically resolved apparent barrier height images closely reflect corresponding topographic constant-current images.

1.4 Tunneling Spectroscopy

Besides the distance and apparent barrier height dependence of the tunneling current there also exists a bias dependence which can be studied by various tunneling spectroscopic methods. For tunneling between metal electrodes in the low-bias limit, the tunneling current is found to be linearly proportional to the applied bias voltage (Eq. (4)). For higher bias and particularly for semiconductor samples, the bias dependence of the tunneling current generally does not exhibit Ohmic behavior, and the constant-current STM images can depend critically on the applied bias (Fig. 7). Studying this bias dependence in detail allows extraction of various spectroscopic information at high spatial resolution, ultimately down to the atomic level. The spectroscopic capability of STM combined with its high spatial resolution is perhaps the most important feature of STM, and has been applied widely, particularly for investigation of semiconductor surfaces [24–26]. Figure 8 shows a simplified one-dimensional potential energy diagram at zero temperature for the system consisting of the tip (left electrode) and the sample (right electrode), which are separated by a small vacuum gap. For zero applied bias (Fig. 8b) the Fermi levels of tip and sample are equal at equilibrium. When a bias voltage U is applied to the sample, the main consequence is a rigid shift of the energy levels downward or upward in energy by an amount $|eU|$, depending on whether the polarity is positive (Fig. 8c) or negative (Fig. 8d). (As discussed in Sec. 2.2.1, we neglect the distortions of the wave functions and the energy eigenvalues due to the finite bias to

a first approximation.) For positive sample bias, the net tunneling current arises from electrons that tunnel from the occupied states of the tip into unoccupied states of the sample (Fig. 8c), whereas at negative sample bias, electrons tunnel from occupied states of the sample into unoccupied states of the tip. Consequently, the bias polarity determines whether unoccupied or occupied sample electronic states are probed. It also becomes clear that the electronic structure of the tip enters as well, as is also obvious from expression (11) for the tunneling current:

$$I \propto \int_0^{eU} n_t(\pm eU \pm \mathscr{E}) n_s(\mathscr{E}) T(\mathscr{E}, e^{rr}) \, d\mathscr{E}$$

By varying the amount of the applied bias voltage, one can select the electronic states that contribute to the tunneling current and, in principle, measure the local electronic density of states. For instance, the current increases strongly if the applied bias voltage allows the onset of tunneling into a maximum of the unoccupied sample electronic density of states. Therefore, the first derivative $dI/dU(U)$ reflects the electronic density of states to a first approximation. However, the energy and bias dependence of the transmission coefficient $T(\mathscr{E}, eU)$ has also to be considered. Since electrons in states with the highest energy 'see' the smallest effective barrier height, most of the tunneling current arises from electrons near the Fermi level of the negatively biased electrode. This has been indicated in Fig. 8 by arrows of differing size. The maximum in the transmission coefficient $T(\mathscr{E}, eU)$ given in Eq. (12) can be written as [26]

$$T_{max}(U) = \exp\left\{-2(s+R) \times \left[\frac{2m}{\hbar^2}\left(\frac{\phi_t + \phi_s}{2} + \frac{|eU|}{2}\right)\right]^{1/2}\right\} \quad (25)$$

The bias dependence of the transmission coefficient typically leads to an order-of-magnitude increase in the tunneling current for each volt increase in magnitude of the applied bias voltage. Since the transmission coefficient increases monotonically with the applied bias voltage, it contributes only a smoothly varying 'background' on which the density-of-states information is superimposed.

As an important consequence of the dominant contribution of tunneling from states near the Fermi level of the negatively biased electrode, tunneling from the tip to the sample (Fig. 8c) mainly probes the empty states of the sample with negligible influence of the occupied states of the tip. On the other hand, tunneling from the sample to the tip is much more sensitive to the electronic structure of the empty states of the tip, which often prevents detailed spectroscopic STM studies of the occupied states of the sample [27].

1.4.1 Scanning Tunneling Spectroscopy at Constant Current

To perform scanning tunneling spectroscopy measurements, a high-frequency sinusoidal modulation voltage can be superimposed on the constant direct current bias voltage applied between the tip and the sample. The modulation frequency is chosen higher than the cut-off frequency of the feedback loop, which keeps the

average tunneling current constant. By recording the tunneling current modulation, which is in-phase with the applied bias voltage modulation, by means of a lock-in amplifier, a spatially resolved spectroscopy signal $\mathrm{d}I/\mathrm{d}U$ can be obtained simultaneously with the constant current image [28, 29]. Based on expression (11) for the tunneling current and by assuming $\mathrm{d}n_t/\mathrm{d}U \approx 0$, one obtains [24]

$$\frac{\mathrm{d}I}{\mathrm{d}U}(U) \propto en_t(0)n_s(eU)T(eU, eU) + \int_0^{eU} n_t(\pm eU \mp \mathscr{E})n_s(\mathscr{E}) \times \frac{\mathrm{d}T(\mathscr{E}, eU)}{\mathrm{d}U}\,\mathrm{d}\mathscr{E} \qquad (26)$$

At a fixed location, the increase of the transmission coefficient with applied bias voltage is smooth and monotonic. Therefore, structure in $\mathrm{d}I/\mathrm{d}U$ as a function of U can usually be attributed to structure in the state density via the first term in Eq. (26). However, interpretation of the spectroscopic data $\mathrm{d}I/\mathrm{d}U$ as a function of position (x, y) is more complicated. As discussed in Sec. 2.3.2 of this Chapter, the apparent barrier height above a local topographic protrusion is larger, that is, the transmission coefficient is smaller, than above a local topographic depression. This spatial variation in the transmission coefficient shows up in spatially resolved measurements of $\mathrm{d}I/\mathrm{d}U$ as a 'background' that is essentially an 'inverted' constant-current topography. Therefore, spectroscopic images corresponding to the spatial variation of $\mathrm{d}I/\mathrm{d}U$ obtained in the constant current mode in fact contain a superposition of topographic and electronic structure information.

1.4.2 Local Spectroscopic Measurements at Constant Separation

To eliminate the influence of the z-dependence of the transmission coefficient, local $I-U$ characteristics can be measured at a fixed tip–sample separation. This is achieved by breaking the feedback circuit for a certain time interval at selected surface locations by means of a sample-and-hold amplifier, while local $I-U$ curves are recorded [30, 31]. The $I-U$ characteristics are usually repeated several times at each surface location and finally signal averaged. Since the feedback loop is inactive while sweeping the applied bias voltage, the tunneling current is allowed to become extremely small. Therefore, band gap states in semiconductors, for instance, can be probed without difficulties. The first derivative $\mathrm{d}I/\mathrm{d}U$ can be obtained from the measured $I-U$ curves by numerical differentiation. The dependence of the measured spectroscopic data on the value of the tunneling conductance I/U can be compensated by normalizing the differential conductance $\mathrm{d}I/\mathrm{d}U$ to the total conductance I/U. The normalized quantity $(\mathrm{d}I/\mathrm{d}U)/(I/U)$ reflects the electronic density of states reasonably well by minimizing the influence of the tip–sample separation [32]. However, the close resemblance of the $(\mathrm{d}\ln I/\mathrm{d}\ln U)-U$ curve to the electronic density of states is generally limited to the position of peaks while peak intensities can differ significantly.

1.4.3 Current Imaging Tunneling Spectroscopy

The measurements of local $I-U$ curves at a constant tip–sample separation can be extended to every pixel in an image, which allows performance of atomically resolved spectroscopic studies [33]. The method, denoted current imaging tunneling spectroscopy (CITS), also uses a sample-and-hold amplifier to alternately gate the feedback control system on and off. During the time of active feedback, a constant stabilization voltage U_0 is applied to the sample, and the tip height is adjusted to maintain a constant tunneling current. When the feedback system is deactivated, the applied sample bias voltage is linearly ramped between two preselected values, and the $I-U$ curve is measured at a fixed tip height. Afterwards, the applied bias voltage is set back to the chosen stabilization voltage U_0 and the feedback system is reactivated. By acquiring the $I-U$ curves rapidly while scanning the tip position at low speed, a constant-current topograph and spatially resolved $I-U$ characteristics can simultaneously be obtained. To increase the possible scan speed and to decrease the amount of data to be stored, one can predefine a coarse grid of pixels in the image at which local $I-U$ curves will be measured (Fig. 9). The ability to probe the local electronic structure down to atomic scale has great potential, for instance, for investigation of surface chemical reactivity on an atom-by-atom basis.

1.5 Spin-Polarized Scanning Tunneling Microscopy

Thus far, the dependence of the tunneling current on the tip–sample separation s, the local barrier height, and the applied sample bias voltage U has been considered:

$$I = I(s, \phi, U) \tag{27}$$

Accordingly, the corresponding modes of STM operation have been discussed: 'topographic' imaging, local barrier height imaging, and tunneling spectroscopy. However, the spin of the tunneling electrons and the additional spin dependence of the tunneling current, if magnetic electrodes are involved, have not yet been considered:

$$I = I(s, \phi, U, \uparrow) \tag{28}$$

By using this spin dependence of the tunneling current in spin-polarized STM (SPSTM) experiments, magnetic information about solid surfaces can be obtained.

Spin-dependent tunneling had been observed in the 1970s using planar tunnel junctions [34–36]. To explain the experimental results, Slonczewski [38] considered a tunnel junction with two ferromagnetic electrodes where the directions of the internal magnetic fields differ by an angle θ (Fig. 10). Within a free-electron model and in the limit of a small applied bias voltage, the following expression for the conductance σ of the ferromagnet/insulator/ferromagnet tunnel junction for the case of two identical ferromagnetic electrodes was found:

$$\sigma = \sigma_{\mathrm{fbf}}(1 + P_{\mathrm{fb}}^2 \cos\theta) \quad |P_{\mathrm{fb}}| \leqslant 1 \tag{29}$$

Here, P_{fb} denotes the effective spin polarization of the ferromagnet/barrier interface and σ_{fbf} is a mean conductance which is proportional to $\exp(-2\kappa s)$. If the ferromagnetic electrodes are different, the conductance becomes

$$\sigma = \sigma_{fbf}(1 + P_{fb}P_{f'b}\cos\theta) \tag{30}$$

For the two special cases of parallel and antiparallel alignment of the internal magnetic field directions, one finds

$$\begin{aligned}\sigma_{\uparrow\uparrow} &= \sigma_{fbf}(1 + P_{fb}P_{f'b}) \\ \sigma_{\uparrow\downarrow} &= \sigma_{fbf}(1 - P_{fb}P_{f'b})\end{aligned} \tag{31}$$

Consequently, one obtains

$$\frac{\sigma_{\uparrow\uparrow} - \sigma_{\uparrow\downarrow}}{\sigma_{\uparrow\uparrow} + \sigma_{\uparrow\downarrow}} = P_{fb}P_{f'b} = P_{fbf} \tag{32}$$

where P_{fbf} is the effective polarization for the whole tunnel junction. An experimental determination of the quantity on the left-hand side of Eq. (32) by means of SPSTM offers a way to derive the effective polarization P_{fbf} locally with a spatial resolution comparable to that of topographic STM images and therefore ultimately on the atomic scale.

The spin dependence of the tunneling current in SPSTM experiments with two magnetic electrodes in a zero external magnetic field was demonstrated by using a ferromagnetic CrO_2 probe tip and a Cr(001) surface [39]. The topological antiferromagnetic order of the Cr(001) surface [40] with alternately magnetized terraces separated by monoatomic steps was confirmed. In addition, a local effective polarization of the CrO_2/vacuum/Cr(001) tunnel junction was derived. Later, atomic resolution in SPSTM experiments has been demonstrated on a magnetite (Fe_3O_4) (001) surface, where the two different magnetic ions Fe^{2+} on the Fe B-sites in the Fe–O (001) planes could be distinguished by using an atomically sharp Fe probe tip prepared in situ [41].

With an additional external magnetic field applied, the magnetization of the sample (or of the tip) can be modulated periodically, for instance, from parallel to antiparallel alignment relative to the tip (or the sample) magnetization direction. Consequently, a portion of the tunneling current is predicted to oscillate at the same frequency, with an amplitude linearly proportional to the average tunneling current [42]. The advantage of this experimental procedure lies in the fact that lock-in detection techniques can be used, resulting in an improvement of the signal-to-noise ratio. In principle, the magnetic field can be modulated at a frequency ν_0 well above the cut-off frequency of the feedback loop, and the corresponding amplitude of the current oscillation at the frequency ν_0 can be recorded with a lock-in amplifier simultaneously with the constant-current topograph. The spatially resolved lock-in signal then provides a map of the effective spin polarization.

A third approach to SPSTM is to use GaAs either as samples [43, 44] or as tips. It is well known that GaAs optically pumped by circularly polarized light provides an efficient source for spin-polarized electrons. On the other hand, one can measure the circular polarization of the recombination luminescence light induced by electrons tunneling from a ferromagnetic counterelectrode.

1.6 Inelastic Tunneling Spectroscopy

Besides elastic tunneling processes, in which the energy of the tunneling electrons is conserved, inelastic tunneling can occur where the electron energy is changed due to interaction of the tunneling electrons

with elementary excitations. In Fig. 11 a potential energy diagram is shown, illustrating elastic and inelastic tunneling processes. In the case of inelastic tunneling, the electron loses a quantum of energy $h\nu_0$ to some elementary excitation mode. According to the Pauli exclusion principle, the final state after the inelastic tunneling event must be initially unoccupied as depicted in Fig. 11a. Consequently, the bias dependence of the tunneling current (Fig. 11b) shows the behavior described below.

Starting from a zero applied bias voltage U, the elastic tunneling current increases linearly proportional to U (Eq. (4)). As long as the applied bias voltage is sufficiently small ($U < h\nu_0/e$, where ν_0 is the lowest energy excitation mode), inelastic tunneling processes cannot occur due to the Pauli exclusion principle. At the threshold bias $U_0 = h\nu_0/e$, the inelastic channel opens up, and the number of electrons which can use the inelastic channel will increase linearly with U (Fig. 11b). Therefore, the total current, including both elastic and inelastic contributions, has a kink at $U_0 = h\nu_0/e$. In the conductance ($\mathrm{d}I/\mathrm{d}U$) versus voltage curve, the kink becomes a step at U_0. Since the fraction of electrons which tunnel inelastically is tiny (typically 0.1–1%), the conductance increase at U_0 due to the onset of the inelastic tunnel channel is too small to be conveniently observed. Therefore, the second derivative ($\mathrm{d}^2I/\mathrm{d}U^2$) is usually measured, which exhibits a peak at U_0. In general, there are many modes which can be excited in the tunneling process. Each excitation mode ν_i contributes a peak in the second derivative $\mathrm{d}^2I/\mathrm{d}U^2(U)$ at the corresponding bias voltage $U_i = h\nu_i/e$ so that $\mathrm{d}^2I/\mathrm{d}U^2(U)$ represents the spectrum of possible excitations. Inelastic electron tunneling can therefore be regarded as a special kind of electron energy loss spectroscopy.

To be able to detect the small changes in tunneling conductance $\Delta G/G$ as a result of the opening of additional inelastic tunneling channels, the relative stability of the tunneling current has to be better than 1%. In addition, low temperatures are required to keep thermal linewidth broadening in the spectra, which is of the order of $k_B T$, small compared with the energy $h\nu$ of the excitation modes, ν being typically a few millielectronvolts.

1.6.1 Phonon Spectroscopy

Electron tunneling between the probe tip and the sample can create phonons at the interface between the conductor and the tunneling barrier. The emission of phonons is believed to take place within a few atomic layers of the interface. Low-temperature STM experiments with a tungsten probe tip and a graphite sample indeed revealed a spectrum of peaks in $\mathrm{d}^2I/\mathrm{d}U^2(U)$ characteristics where the positions of the peaks corresponded closely to the energies of the phonons of the graphite sample and the tungsten tip [46]. The measured increase in conductance at the phonon energies was of the order of 5%. By analogy with elastic scanning tunneling spectroscopy (see Sec. 1.4.1), spectroscopic imaging can be performed by recording $\mathrm{d}^2I/\mathrm{d}U^2$ at a particular phonon energy while scanning the tip over the sample surface. This method allows one to map spatial variations of the phonon spectra, caused by spatial varia-

tions in the coupling between the tunneling electrons and the phonons, on the atomic scale.

1.6.2 Molecular Vibrational Spectroscopy

Inelastic tunneling spectroscopy can also yield information about vibrational modes of molecules adsorbed on a surface. By using low-temperature STM, a vibrational spectrum of an individual adsorbed molecule can be obtained by positioning the probe tip over the preselected adsorbate. It is even possible to form a map showing the sites within a molecule where particular resonances occur.

For sorbic acid adsorbed on graphite, a spectrum of strong peaks was observed in the first derivative dI/dU instead of the expected second derivative d^2I/dU^2 [47]. The energies of the peaks corresponded approximately to the vibrational modes of the molecule. The measured increase in conductivity at the molecular resonances was as much as a factor of 10, which is at least two orders of magnitude larger than expected.

Future inelastic tunneling experiments have to focus on the assignment of characteristic features in the tunneling spectra to particular molecular functional groups. This will probably help to identify chemical species by STM, a problem which is not solvable by elastic tunneling spectroscopy.

Acknowledgments

The author would like to acknowledge all colleagues who provided illustrations for this Chapter.

1.7 References

[1] G. Binnig, H. Rohrer, Ch. Gerber, E. Weibel, *Phys. Rev. Lett.* **1982**, *49*, 57.
[2] G. Binnig and H. Rohrer, *Helv. Phys. Acta* **1982**, *55*, 726.
[3] G. Binnig and H. Rohrer, *Rev. Mod. Phys.* **1987**, *59*, 615.
[4] R. Wiesendanger, *Scanning Probe Microscopy and Spectroscopy: Methods and Applications*, Cambridge University Press, Cambridge **1994**.
[5] J. Bardeen, *Phys. Rev. Lett.* **1961**, *6*, 57.
[6] J. Tersoff, D. R. Hamann, *Phys. Rev. Lett.* **1983**, *50*, 1988.
[7] J. Tersoff, D. R. Hamann, *Phys. Rev. B* **1985**, *31*, 805.
[8] C. J. Chen, *J. Vac. Sci. Technol.* **1988**, *A6*, 319.
[9] S. Ohnishi, M. Tsukada, *J. Vac. Sci. Technol.* **1990**, *A8*, 174.
[10] C. J. Chen, *Phys. Rev. B* **1990**, *42*, 8841.
[11] C. J. Chen, *J. Vac. Sci. Technol.* **1991**, *A9*, 44.
[12] N. D. Lang, *Phys. Rev. Lett.* **1985**, *55*, 230.
[13] N. D. Lang, *Phys. Rev. Lett.* **1986**, *56*, 1164.
[14] N. D. Lang, *IBM J. Res. Develop.* **1986**, *30*, 374.
[15] Y. Kuk, P. J. Silverman, H. Q. Nguyen, *J. Vac. Sci. Technol.* **1988**, *A6*, 524.
[16] J. Wintterlin, J. Wiechers, H. Brune, T. Gritsch, H. Höfer, R. J. Behm, *Phys. Rev. Lett.* **1989**, *62*, 59.
[17] M. Bode, R. Pascal, R. Wiesendanger, ~~to be published~~ Z. Phys. B
[18] V. M. Hallmark, S. Chiang, J. F. Rabolt, J. D. Swalen, R. J. Wilson, *Phys. Rev. Lett.* **1987**, *59*, 2879.
[19] A. Baratoff, *Physica B* **1984**, *127*, 143.
[20] C. J. Chen, *Phys. Rev. Lett.* **1990**, *65*, 448.
[21] G. Binnig, N. Garcia, H. Rohrer, J. M. Soler, F. Flores, *Phys. Rev. B* **1984**, *30*, 4816.
[22] J. H. Coombs, M. E. Welland, J. B. Pethica, *Surf. Sci.* **1988**, *198*, L353.
[23] G. Binnig, H. Rohrer, *Surf. Sci.* **1983**, *126*, 236.
[24] R. J. Hamers, *Annu. Rev. Phys. Chem.* **1989**, *40*, 531.
[25] R. M. Tromp, *J. Phys. C: Condens. Matter* **1989**, *1*, 10211.
[26] R. M. Feenstra, *NATO ASI Ser. E: Appl. Sci.* **1990**, *184*, 211.
[27] T. Klitsner, R. S. Becker, J. S. Vickers, *Phys. Rev. B* **1990**, *41*, 3837.

[28] G. Binnig, K. H. Frank, H. Fuchs, N. Garcia, B. Reihl, H. Rohrer, F. Salvan, A. R. Williams, *Phys. Rev. Lett.* **1985,** *55*, 991.
[29] R. S. Becker, J. A. Golovchenko, D. R. Hamann, B. S. Swartzentruber, *Phys. Rev. Lett.* **1985,** *55*, 2032.
[30] R. M. Feenstra, W. A. Thompson, A. P. Fein, *Phys. Rev. Lett.* **1986,** *56*, 608.
[31] J. S. Stroscio, R. M. Feenstra, A. P. Fein, *Phys. Rev. Lett.* **1986,** *57*, 2579.
[32] R. M. Feenstra, J. A. Stroscio, *Phys. Scripta* **1987,** *T19*, 55.
[33] R. J. Hamers, R. M. Tromp, J. E. Demuth, *Phys. Rev. Lett.* **1986,** *56*, 1972.
[34] P. Avouris, I.-W. Lyo in *Chemistry and Physics of Solid Surfaces VIII. Springer Series in Surface Sciences*, Vol. 22 (Eds.: R. Vanselow, R. Howe), Springer, Berlin, **1990,** p. 371.
[35] P. M. Tedrow, R. Meservey, *Phys. Rev. Lett.* **1971,** *26*, 192.
[36] M. Julliere, *Phys. Lett. A* **1975,** *54*, 225.
[37] S. Maekawa, U. Gäfvert, *IEEE Trans. Magn.* **1982,** *18*, 707.
[38] J. C. Slonczewski, *Phys. Rev. B* **1989,** *39*, 6995.
[39] R. Wiesendanger, H.-J. Güntherodt, G. Güntherodt, R. J. Gambino, R. Ruf, *Phys. Rev. Lett.* **1990,** *65*, 247.
[40] S. Blügel, D. Pescia, P. H. Dederichs, *Phys. Rev. B* **1989,** *39*, 1392.
[41] R. Wiesendanger, I. V. Shvets, D. Bürgler, G. Tarrach, H.-J. Güntherodt, J. M. D. Coey, *Europhys. Lett.* **1992,** *19*, 141.
[42] M. Johnson, J. Clark, *J. Appl. Phys.* **1990,** *67*, 6141.
[43] S. F. Alvarado, P. Renaud, *Phys. Rev. Lett.* **1992,** *68*, 1387.
[44] K. Sueoka, K. Mukasa, K. Hayakawa, *Jpn. J. Appl. Phys.* **1993,** *32*, 2989.
[45] P. K. Hansma, *Phys. Rep.* **1977,** *30*, 145.
[46] D. P. E. Smith, G. Binnig, C. F. Quate, *Appl. Phys. Lett.* **1986,** *49*, 1641.
[47] D. P. E. Smith, M. D. Kirk, C. F. Quate, *J. Chem. Phys.* **1987,** *86*, 6034.

Figure 1. Schematic set-up for STM.

Figure 2. Microscopic view of the STM imaging mechanism. (Image courtesy of Chen [11].)

Figure 3. (a) Current density for the case in which a sodium atom is adsorbed on the left electrode. The length and thickness of the arrow are proportional to $\ln(ej/j_0)$ evaluated at the spatial position corresponding to the center of the arrow (1 B = 0.529 Å). (Image courtesy of Lang [14].) (b) Change in tip distance versus lateral separation for constant tunnel current. The tip atom is sodium; sample adatoms are sodium, sulfur, and helium. (Image courtesy of Lang [13].)

Figure 4. Dependence of the measured corrugation on the size of the cluster on the tip for Au(110) (2 × 1) and Au(100) (5 × 1) reconstructed surfaces. (Image courtesy of Kuk [15].)

Figure 5. (a) STM topograph of the W(110)/C-R(15 × 3) reconstructed surface obtained with a tunneling gap resistance $R = 2.11 \times 10^6\,\Omega$. (b) Corresponding STM topograph with a tunneling gap resistance $R = 1.72 \times 10^{10}\,\Omega$ [17].

Figure 6. The image-reduced mean barrier height (full line) and the apparent barrier height deduced from the $\ln I$–s relation for this barrier (dotted line). The work function used in the calculation is 4.5 eV. It can be seen that the apparent barrier height is always within 0.2 eV of the work function despite the collapse of the image-reduced barrier. (Image courtesy of Coombs [22].)

Figure 7. (a) STM topograph of the Si(111)7 × 7 reconstructed surface with a step along which molecules were found to be preferentially adsorbed. The image was taken with negative sample bias voltage polarity. (b) Corresponding STM image obtained with positive sample bias voltage polarity. The adsorbed molecules have become almost invisible. The Si(111)7 × 7 surface also appears different depending on the bias voltage polarity [17].

Figure 8. Energy level diagrams for the sample and the tip. (a) Independent sample and tip. (b) Sample and tip at equilibrium, separated by a small vacuum gap. (c) Positive sample bias: electrons tunnel from the tip to the sample. (d) Negative sample bias: electrons tunnel from the sample into the tip. (Image courtesy of Hamers [24].)

Figure 9. STM topograph of the unoccupied states of an Si(111)7 × 7 surface (sample bias 2 V). The atoms imaged are the top-layer Si adatoms. The grid encompasses a 14 × 14 Å area of this surface for which tunneling spectra have been obtained. The 100 tunneling spectra are plotted in the dI/dU form. Such spectral maps allow one not only to obtain the energies of the occupied (negative bias) and unoccupied (positive bias) states of particular atomic sites, but also to obtain information on the spatial extent of their wave functions. (Image courtesy of Avouris [34].)

Figure 10. Schematic potential diagram for two metallic ferromagnets separated by an insulating barrier. The molecular fields h_A and h_B within the magnets form an angle θ. (Image courtesy of Slonczewski [38].)

Figure 11. Tunneling electrons can excite a molecular vibration of energy $h\nu$ only if $eU > h\nu$. For smaller voltages there are no vacant final states for the electrons to tunnel into. Thus the inelastic current has a threshold at $U = h\nu/e$. The increase in conductance at this threshold is typically below 1%. A standard tunneling spectrum, d^2I/dU^2 versus U, accentuates this small increase; the step in dI/dU becomes a peak in d^2I/dU^2. (Image courtesy of Hansma [45].)

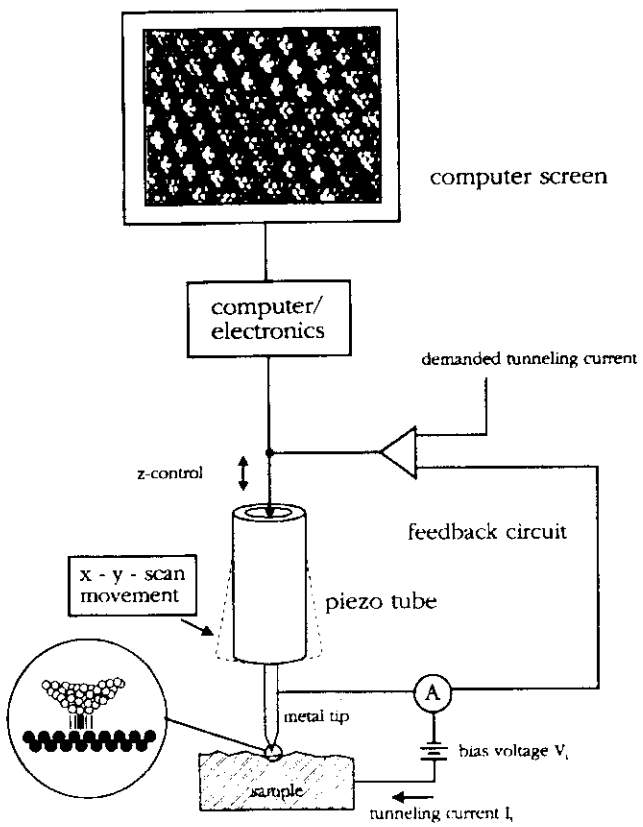
computer screen
computer/
electronics
demanded tunneling current
z-control
feedback circuit
x - y - scan
movement
piezo tube
A
metal tip
bias voltage V
sample
tunneling current I

55%

Vc 1 Fl. 1

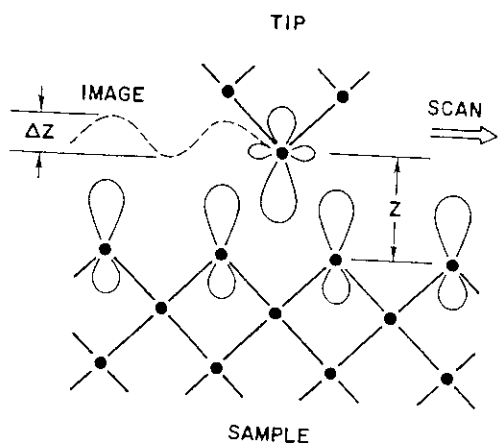

40%

Σ 1

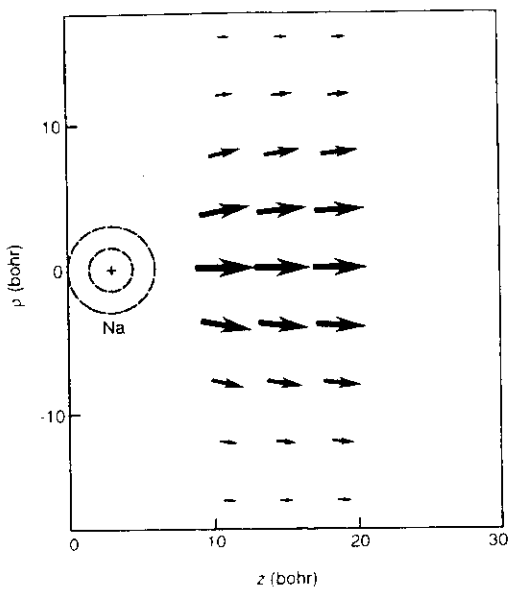
10
0
-10
ρ (bohr)
Na
0
10
20
30
z (bohr)

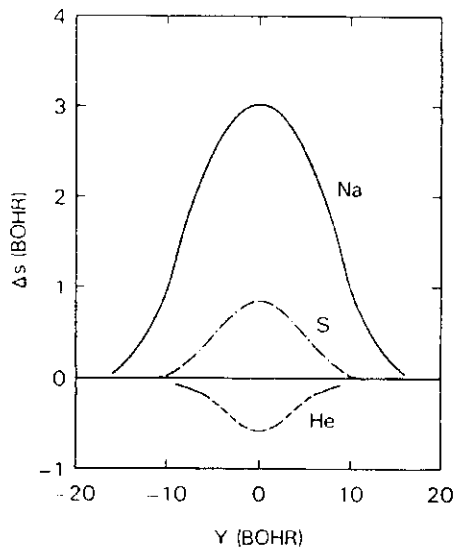

90%

Fig. 3b

Vol II ch VI 1

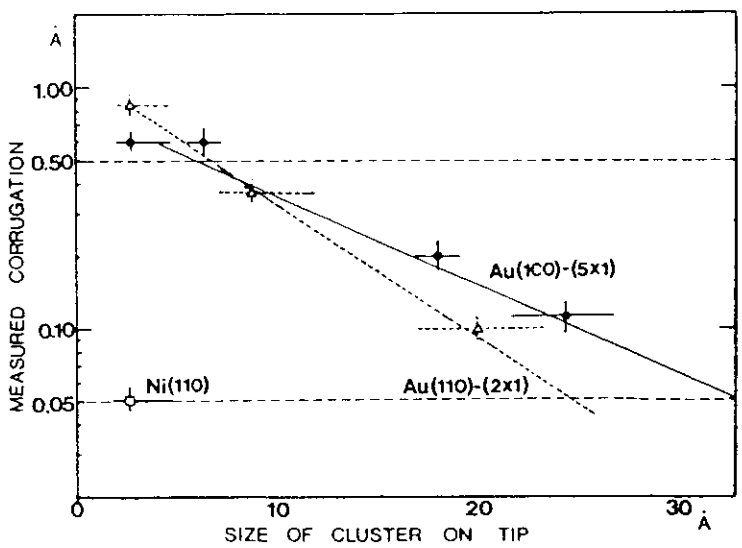

Fig. 4 100%

R. Wiesendanger

Vol 1 Ch VII 1

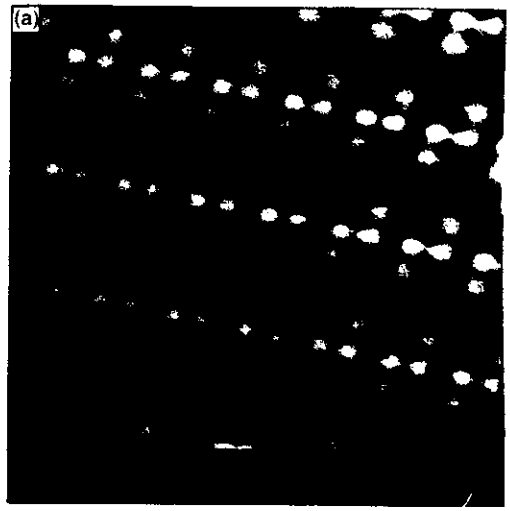

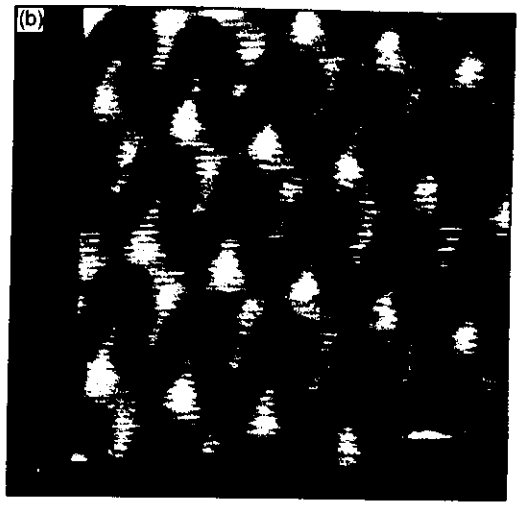

66%

Fig. 1

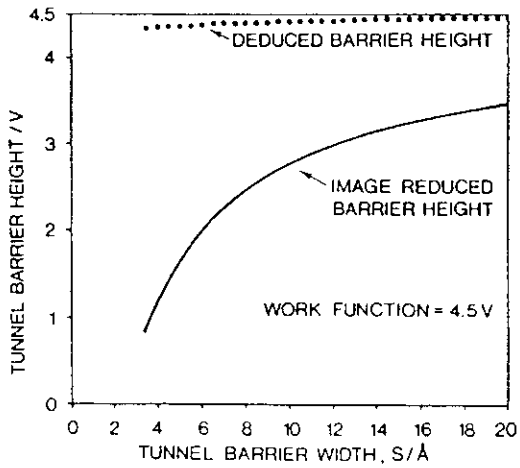
DEDUCED BARRIER HEIGHT
IMAGE REDUCED BARRIER HEIGHT
WORK FUNCTION = 4.5 V
TUNNEL BARRIER HEIGHT / V
TUNNEL BARRIER WIDTH, S/Å
0
1
2
3
4
4.5
0
2
4
6
8
10
12
14
16
18
20

Fig 6 79%

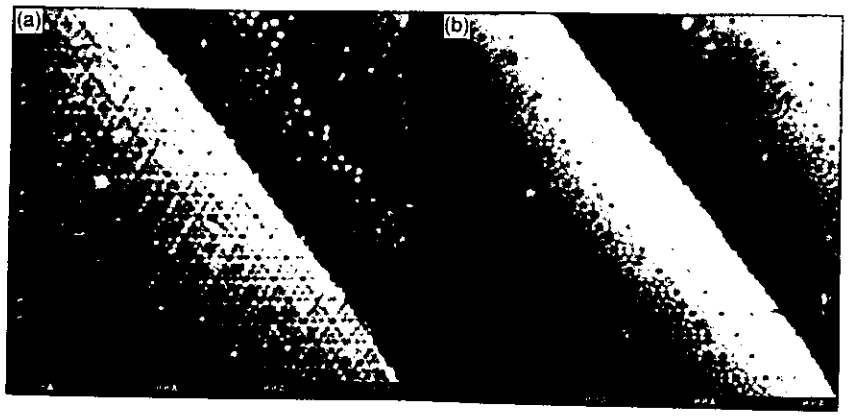

65%

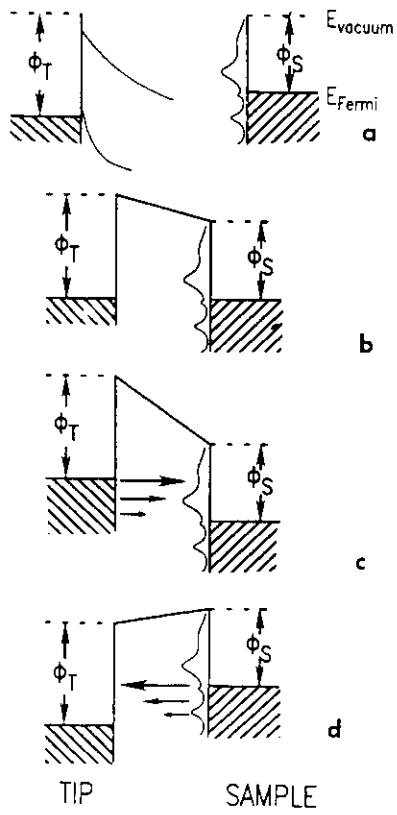
E_{vacuum}
Φ_T
Φ_S
E_{Fermi}
a
b
c
d
TIP
SAMPLE

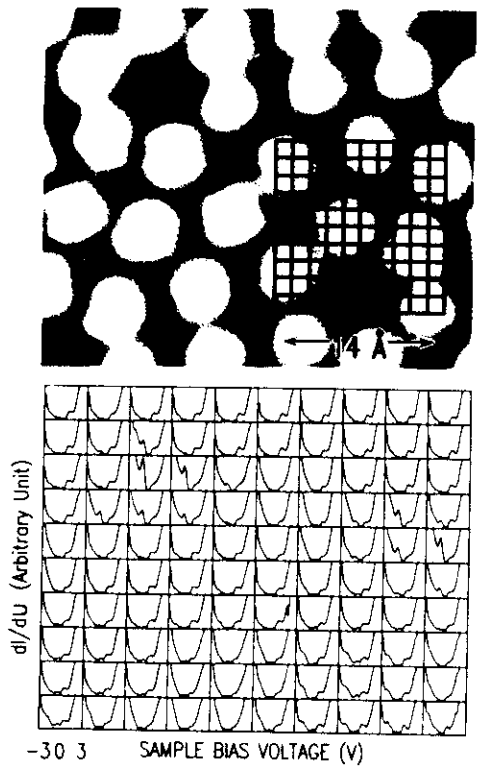
4 Å
dI/dU (Arbitrary Unit)
-3 0 3
SAMPLE BIAS VOLTAGE (V)

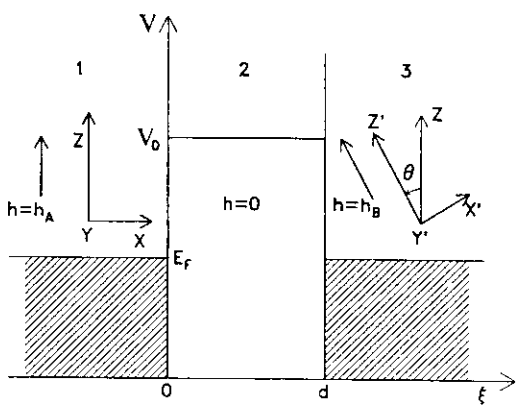
V
1
2
3
Z
V_0
h=h_A
Y
X
h=0
E_f
Z'
Z
θ
h=h_B
X'
Y'
0
d
ξ

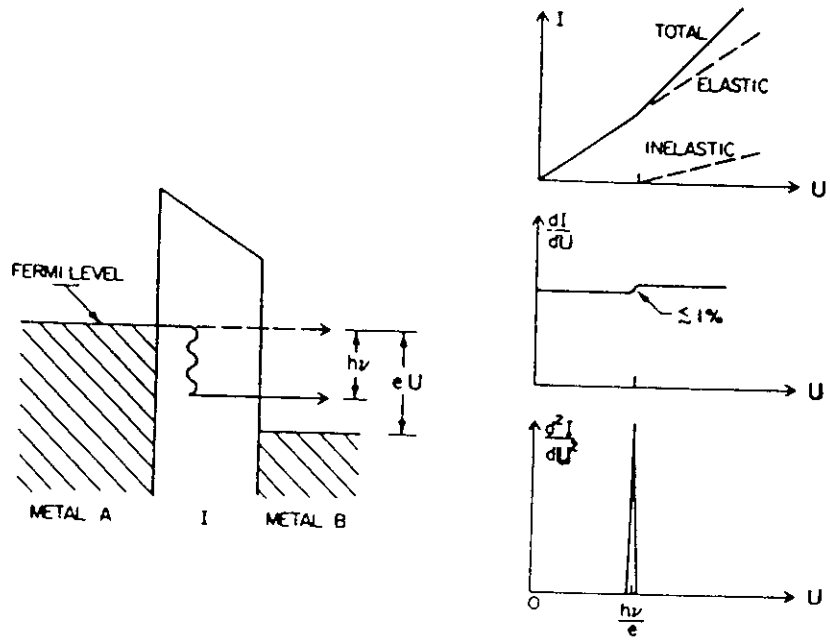

100 %

Fig. 11

R Wiesendanger

Vol Ch VII, 1